ELSEVIER

Covalently anchoring covalent organic framework on carbon nanotubes for highly efficient electrocatalytic CO_2 reduction

Hong Dong [a,b,1], Meng Lu [c,1], Ya Wang [a,1], Hong-Liang Tang [a], Di Wu [a], Xiaojun Sun [a], Feng-Ming Zhang [a,*]

[a] *School of Material Science and Chemical Engineering, Harbin University of Science and Technology, Harbin 10040, PR China*
[b] *State Key Laboratory of Catalysis, Dalian National Laboratory for Clean Energy, Dalian Institute of Chemical Physics, Chinese Academy of Sciences, Dalian 116023, PR China*
[c] *School of Chemistry, South China Normal University, Guangzhou 510006, PR China*

ARTICLE INFO

ABSTRACT

Porphyrin-based covalent organic frameworks (Por-COF) nanosheets were vertically anchored on carbon nanotubes (CNT) with covalent connection for efficient electrocatalytic CO_2 reduction reaction (CO_2RR). The CNT not only acts as ideal carriers for the dispersion of Pro-COF but also facilitates electron transfer along porphyrin planes to immobilized metal active sites. As a result, covalently linked MWCNT-Por-COF-M (M: Co, Ni, Fe) display improved electrocatalytic CO_2-to-CO activity and selectivity compared to pure Por-COF-M and MWCNT@Por-COF-M without covalent connection between two components. In particular, MWCNT-Por-COF-Co exhibits superior activity (FE_{CO}: 99.3%), higher partial current density and good durability in 0.5 M $KHCO_3$ by H-type cell, while MWCNT-Por-COF-Cu exhibits the highest CH_4 faradaic efficiency of 71.2% in 1.0 M KOH by flow cell. The results of HRTEM and Auger spectrum revealed that the high performance of MWCNT-Por-COF-Cu could be attributed to the generated Copper-based nanoclusters during the electrocatalytic CO_2RR process.

1. Introduction

Global energy demands and environment issues support broad research interest in CO_2 reduction reaction (CO_2RR) for its ideal way to realize recycling utilization of carbon resources [1–6]. Within this context, electrocatalytic CO_2RR offers a potential approach for sustainable and efficient conversion of CO_2 to value-added carbon products [7–16]. However, owing to the inherent thermodynamic stability of C=O chemical bond in CO_2 (750 kJ mol^{-1}) [17], electrocatalytic CO_2RR generally needs to overcome a high activation barrier. Moreover, the competitive reaction of hydrogen evolution reaction (HER) and the similar redox potentials of various CO_2RR products usually result in poor selectivity and low conversion efficiency, which limit their practical application [18,19]. To solve these issues, researchers have explored different types of electrocatalytic CO_2RR materials, such as metals [20, 21], metal dichalcogenide [22], transition metal oxide [23,24] and metal-free 2D materials (g-C_3N_4) [25]. In spite of the tremendous efforts and glorious achievements, the studies in this field still have some challenges, such as weak CO_2 adsorption and activation capacity of catalysts, slow reaction kinetics, low electron transmission efficiency and poor product selectivity [26,27].

Covalent-organic frameworks (COFs), as a new class of crystalline and porous material has recently attracted enormous attention for their variety of applications including gas storage [28,29], chemical sensing [30], drug delivery [31,32] and catalysis [33] due to their well-defined structure, high stability and inherent porosity [34,35]. In the past few years, COFs have appeared as a new kind of electrocatalytic CO_2RR materials by incorporating metal ions as active sites. Especially, the excellent electrocatalytic CO_2RR activities of some porphyrin-based COFs, such as COF-366, COF-367, TTCOF, have been confirmed in pioneer works for the electronic character of porphyrin active sites and high charge carrier mobility along porphyrin plane [36–42]. Although this encouraging progress, the inefficient electrical conduction between layers generally results in low electron transmission efficiency in most of bulk COFs materials, which limits further enhancing their electrocatalytic CO_2RR activity. Thus, rationally integrating COFs with conductive support to construct COF-based composite materials with effective electron transfer capability holds interesting prospects for

---

highly efficient electrocatalytic CO_2RR. However, this strategy of combining COFs and conductive support for electrocatalytic CO_2RR has not been systematically explored.

As one of the most famous conductive material, carbon nanotubes (CNT) are a promising candidate for supporting various catalysts due to their intrinsic physical properties including superior mechanical strength and electrical conductivity [43–45], which can provide consecutive tunneling for electron transfers. Multiple molecular catalysts (such as metalloprophyrin and metallophthalocyanine etc.) have been immobilized on CNT by π-π interaction for efficient electrocatalytic CO_2 conversion [46–48]. Differently from the immobilized molecular catalysts on CNT, 2D COFs are assembled with congugated multilayer. We reasoned, the combination of CNT and COFs by π-π interaction may lead to relatively high resistance of electron transfer by accrossing COFs interlayser, while controlling the combination mode of CNT and COFs to realize electron conduction along porphyrin-based plane of COFs should be benifitial for the transfer of electrons to metal active sites. Moreover, a strong bonded connection of COFs and CNT that can facilitate electron transfer from CNT to COFs layers is also essential for high electrocatalytic performance of the resulatant material as well as the solid integration of them.

Based on the above consideration, we integrate Por-COF with CNT by covalent bonds constructing a series of covalently connected MWCNT-Por-COF-M for efficient electrocatalytic CO_2RR. To realize the formation of covalent bonds between CNT and Por-COF and effective electron transmission along porphyrin-based plane of Por-COF, -NH_2 group modified MWCNT was chosen to bond Pro-COF and disperse Pro-COF nanosheets by in-situ reaction. As a result, ultra-small Por-COF nanosheets were covalent anchored on the surface of MWCNT with uniform dispersion (Scheme 1). After chelating different metal ions, a series of MWCNT-Por-COF-M show higher electrocatalytic CO_2-to-CO activity and selectivity compared to pure Por-COF-M. In particular, the MWCNT-Por-COF-Co shows the highest CO Faraday efficiency up to 99.3% at the potential of − 0.6 V and a current density of 18.77 mA cm^{-2} at − 1.0 V.

Further experiments clarified that the superior electrocatalytic activity of MWCNT-Por-COF-Co is mainly attributed to more efficient electron transfer during the CO_2RR reaction process. Furthermore, we also investigated the electrocatalytic CO_2 reduction activity of MWCNT-Por-COF-Cu in 1.0 M KOH by flow cell. The results show that MWCNT-Por-COF-Cu exhibits the highest CH_4 faradaic efficiency of 71.2%. The results of HRTEM and Auger spectrum revealed that the high performance of MWCNT-Por-COF-Cu could be attributed to the generated Copper-based nanoclusters during the electrocatalytic CO_2RR process.

2. Experimental section

2.1. Materials

All of the reagents and solvents were commercially available and used without further purification. Por-CHO (≥98%) was purchased from Jilin Chinese Academy of Sciences-Yanshen Technology Co., Ltd.

2.2. Instrumentation

Infrared spectrum using the KBr pellet was measured on a Bruker Tensor 27 in the range of 4000–400 cm^{-1}. Scanning electron microscopy (SEM) micrographs were recorded on a Hitachi S-4800 instrument operating at 20 kV. Transmission electron microscope (TEM) images were taken on a JEM-2100 microscope equipped. X-ray powder diffraction (PXRD) patterns were recorded on a DX-2700B X-ray diffractmeter. The patterns were collected at a scanning rate of 5° per min in the 2θ range from 5° to 50°. Nitrogen adsorption-desorption isotherms were measured at 77 K on a Micromeritics ASAP 2020 adsorptometer, and CO_2 adsorption isotherms were measured at 298 K. X-ray photoelectron spectroscopy (XPS) study was performed on the Kratos Axis Ultra DLD.
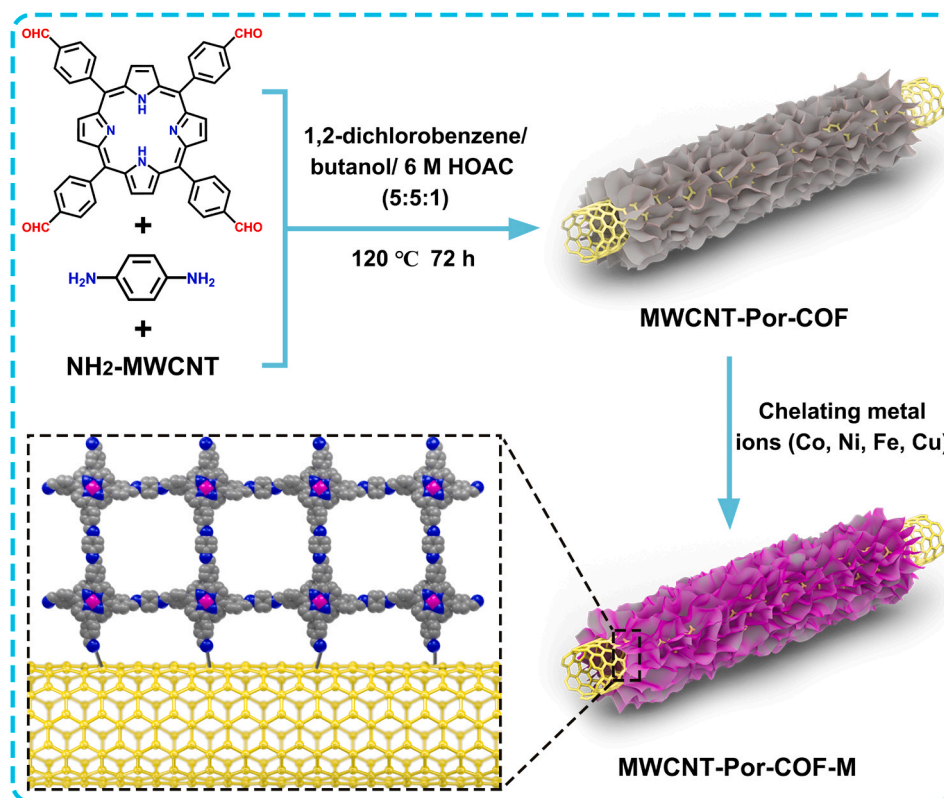
Scheme 1. . Schematic diagram of synthetic process of the MWCNT-Por-COF-M (M: Co, Ni, Fe, Cu) composite materials.

2.3. Synthesis of Por-COF

According to previous reported procedures [38]. A vacuum valve measuring o.d×i.d. = 19 × 8 mm^2 and length 65 mm was charged with Por-CHO (72.6 mg, 0.10 mmol), *p*-phenylenediamine (21.6 mg, 0.20 mmol), 2.5 mL butanol, 2.5 mL 1,2-dichlorobenzene, and 0.5 mL of 6 mol/L aqueous acetic acid. This solution was then sonicated for 20 min to form a homogeneous dispersion. Afterwards, the vacuum valve was flash frozen in a liquid N$_2$ bath (77 K) and degassed by three freeze-pump-thaw cycles, sealed under vacuum, and then heated at 120 °C for 3 days. The products were collected by centrifugation or filtration and washed with anhydrous THF (50 mL) for three times. The powders collected were soaked in anhydrous acetone for 48 h, replaced the solvent for 5–6 times and then dried at 180 °C for 12 h under vacuum to afford Por-COF materials.

2.4. Synthesis of MWCNT-Por-COF

A vacuum valve measuring o.d×i.d. = 19 × 8 mm^2 and length 65 mm was charged with Por-CHO (40 mg), different quality of NH$_2$-MWCNT (30, 50, 70, 90, 120 mg), 2.5 mL butanol, and 2.5 mL 1,2-dichlorobenzene. This solution was then sonicated for 20 min to form a homogeneous dispersion solution. Then *p*-phenylenediamine (10.08 mg, 0.10 mmol) was added in above homogeneous solution and continue sonicated for 20 min. Finally, 0.5 mL of 6 mol/L aqueous acetic acid was added in above homogeneous solution. Afterwards, the vacuum valve was flash frozen in a liquid N$_2$ bath (77 K) and degassed by three freeze-pump-thaw cycles, sealed under vacuum, and then heated at 120 °C for 3 days. The products were collected by centrifugation or filtration and washed with anhydrous THF (50 mL) for three times. The powders collected were soaked in anhydrous acetone for 48 h, replaced the solvent for 5–6 times and then dried at 180 °C for 12 h under vacuum to afford different weight ratios of NH$_2$-MWCNT(X)-Por-COF composite materials.

2.5. Synthesis of various MWCNT-Por-COF-M

CoCl$_2$.6 H$_2$O (100 mg) (or FeCl$_2$.4 H$_2$O, NiCl$_2$.6 H$_2$O, CuCl$_2$.6 H$_2$O), MWCNT-Por-COF (50 mg), and Tetrahydrofuran (THF) (40 mL) were mixed and heated at 50 °C for 15 h. The powder was collected by filtration and washed with THF and acetone for several times. Finally, the powder was dried in vacuum at 120 °C for 48 h. For NiCl$_2$.6 H$_2$O, the THF was replaced with acetonitrile (CH$_3$CN), because NiCl$_2$.6 H$_2$O is insoluble in THF.

2.6. Synthesis of amino-free functionalized MWCNT@Por-COF-Co

MWCNT@Por-COF-Co composite material was prepared by the above method except that was amino-free functionalized MWCNT replaced by NH$_2$-MWCNT.

2.7. Electrochemical measurements of H-type cell

The H-type cell tests of the catalysts were performed at ambient environment on the electrochemical workstation (CHI660E) in a standard three-electrode configuration in 0.5 M KHCO$_3$. Carbon rod and Ag/AgCl electrode were used as the counter and reference electrode, respectively. The experiment was performed in an airtight electrochemical H-type cell with a catalyst-modified carbon cloth electrode (CCE, 1 cm × 2 cm) as the work electrode. Nafion solution was introduced as a kind of electrocatalyst dispersion solution, which can form a homogeneous ink with MWCNT-Por-COF-M and further help to attach onto the surface of carbon cloth. The preparation procedures of the CCE working electrode were presented as follows: 10 mg electrocatalyst, and 1 mL 0.5% Nafion solution were grounded to form uniform catalyst ink. After sonication for 30 min, the ink was dropped directly onto a carbon

cloth (1 cm × 1 cm) with a catalyst loading density of ~1 mg cm^{-2} and dried. In the H-type cell, two compartments were separated by an exchange membrane (Nafion®117). During the electrocatalytic CO$_2$RR experiments, the polarization curves were performed by LSV mode at a scan rate of 2 mV s^{-1}. Initially, polarization curves for the modified electrode were recorded under an inert N$_2$ atmosphere. After that, the solution was bubbled with CO$_2$ (99.999%) for at least 30 min to make the aqueous solution saturated and then the electrocatalytic CO$_2$RR test was conducted. Potential was measured vs. Ag/AgCl electrode and the results were reported vs. RHE based on the Nernst equation: E (vs. RHE) = E (vs. Ag/AgCl) + 0.1989 V + 0.059 × pH. EIS spectroscopy measurement was carried out by applying an AC voltage with 10 mV amplitude in a frequency range from 1000 kHz to 100 mHz at overpotential of − 0.7 V (vs. RHE). To estimate the ECSA, CV were tested by measuring Cdl under the potential window range from 0 V to 0.1 V (vs. RHE) with various scan rates from 10 to 100 mV s^{-1}. All the LSV curves were presented without iR compensation.

2.8. Electrochemical measurements of flow cell

CO$_2$ electrolysis was performed in a three-channel flow cell composed of a gas-diffusion layer (GDL), an anion exchange membrane (Fumasep, FAA-3-PK-130) and a Pt plate (1 cm^2) anode as shown in Scheme S1. The prepared catalyst and gas-diffusion layer, anion exchange membrane and Pt anode were clamped together in order using polytetrafluoroethylene (PTFE) spacers and then fixed with screws. The electrolyte (1.0 M KOH aqueous solution) was then introduced into the chamber between membrane and the cathode as well as the chamber between the anode and membrane. The electrolyte in cathode and anode were circulated by a peristaltic pump (LongerPump, BT100–2 J), with the flow rate of 5 mL min^{-1}. The high-purity CO$_2$ (99.999%) gas was continuously passed through the flow chamber which is behind the gas-diffusion layer and diffuse into the electrolyte present at the catalyst. The gas flow rate was set as 20 sccm via a mass flow controller (AITOLY, MFC300). A saturated Ag/AgCl reference electrode (CHI111) was located in the catholyte stream and positioned ≈ 1 cm from the cathode was used to measure the cathodic half-cell potential.

2.9. Reaction product analysis and calculation

The electrolysis was carried out in an airtight electrochemical H-type cell at selected potentials (−0.5 to −1.0 V) to determine the reduction products and their Faradic efficiency. The gaseous reduction products (e.g., CO) were monitored by a GC (GC-7920) equipped with a flame ionization detector. During the test, nitrogen was the carrier gas. A TCD was used to analyze hydrogen with nitrogen as the carrier gas. The liquid products were collected from the cathode chambers after electrolysis and detected by IC spectroscopy.

The calculation of Faradaic efficiency.

For CO,

$$FE = \frac{2n_{CO} \times F}{Q} \times 100\% \tag{1}$$

For H$_2$,

$$FE = \frac{2n_{H_2} \times F}{Q} \times 100\% \tag{2}$$

where F is the Faraday constant (F = 96485 C/mol), n$_{CO}$ is the moles of produced CO, Q is the total charge (C), and n$_{H2}$ is the moles of produced H$_2$.

The faradaic efficiencies for flow cell were calculated using the following equation:

$$FE = \frac{nFxV}{j_{Tot}} \tag{3}$$

Where n = number of electrons transferred.

F = Faraday's constant.

x = mole fraction of product.

V = total molar flow rate of gas.

j_{Tot} = total current.

Turnover frequency (TOF, s^{-1}).

The TOF for CO was calculated as follows:

$$TOF = \frac{i \times FE_{CO}}{2F \times n_{cat}} \qquad (4)$$

where i is the current, n_{cat} is the total moles of catalyst employed in the electrolysis.

The calculation of energy efficiency (EE)

$$EE = \frac{E_{CO} \times FE_{CO}}{E_{CO} + \eta} \times 100\% \qquad (5)$$

where E_{CO} (V) is the equilibrium cell potential for CO, FE_{CO} (%) is the Faradaic efficiency of CO, η (V) is the overpotential.

3. Results and discussion

3.1. Preparation process and structure characterization

Por-COF was synthesized by condensing 5,10,15,20-Tetrakis(4-benzaldehyde)porphyrin (Por-CHO) and p-phenylenediamine in a mixture of butanol/1,2-dichlorobenzene/AcOH (5:5:1) under solvothermal conditions [49]. Fourier-transform infrared (FT-IR) spectrum of Por-COF shows a new peak at 1617 cm^{-1} attributed to the formation of C=N bond (Fig. S1), along with the dismissing of characteristic bands of -CHO (1700 cm^{-1}) group in Por-CHO and -NH$_2$ (3369 cm^{-1}) in *p*-phenylenediamine. In addition, the powder X-ray diffraction (PXRD) pattern of Por-COF matches well with the simulated PXRD pattern indicating successful synthesis of Por-COF (Fig. S2). A series of covalently connected MWCNT(X)-Por-COF (X = 50, 62, 70, 75, 80 wt%) composites with different contents of MWCNT were synthesized by adding variably quantitative NH$_2$-MWCNT into the above reaction system of Por-COF. The PXRD patterns of MWCNT(X)-Por-COF support the successful synthesis of these composites for the appearance of a new peak at 28 degrees from MWCNT (Fig. S2). The resultant MWCNT-Por-COF-M (X = 70 wt%, M: Co, Ni, Fe) composites were obtained by coordinating different transition metal ions (Co^{2+}, Ni^{2+}, Fe^{2+})
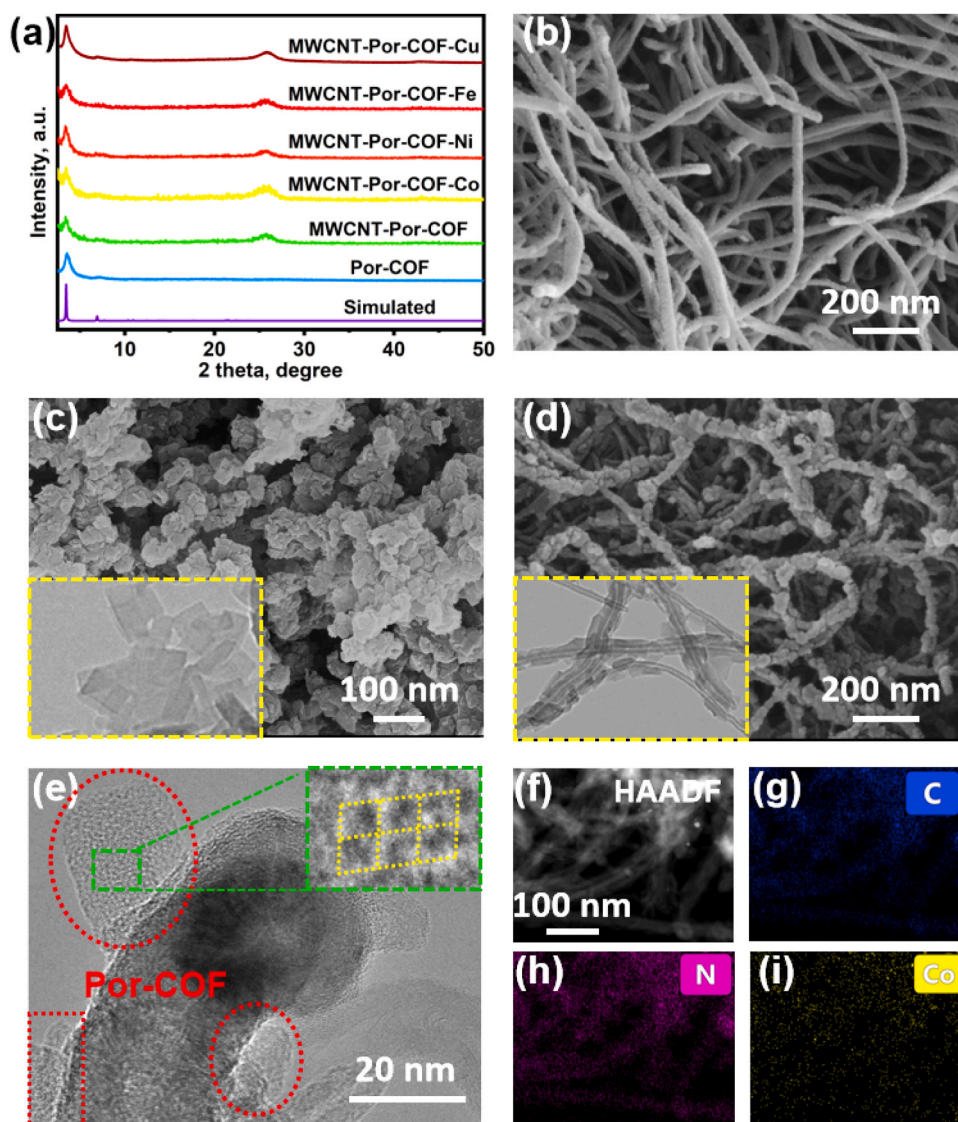
Fig. 1. (a) PXRD patterns of MWCNT-Por-COF-M (M: Co, Ni, Fe, Cu). (b-d) SEM and TEM (inset) images of NH$_2$-MWCNT, Por-COF and MWCNT-Por-COF. (e) HRTEM image and pores (inset) of MWCNT-Por-COF. (f-i) HAADF and elements mapping images of MWCNT-Por-COF-Co.

onto porphyrin moiety of these materials. As presented in Fig. 1a, the PXRD patterns of MWCNT-Por-COF-M (Co, Ni, Fe, Cu) agree well with the parent Por-COF, and the main peaks in FT-IR spectra of MWCNT-Por-COF-M also do not change apparently (Fig. S3). XPS measurements of MWCNT-Por-COF-M (M: Co, Ni, Fe) confirm that the metal centers in MWCNT-Por-COF-M are all bivalence (Fig. S4-S6). The Cu 2p XPS clearly demonstrated that MWCNT-Por-COF-Cu displays two peaks at the binding energy of 935.0 and 954.8 eV attributed to Cu $2p_{3/2}$ and Cu $2p_{1/2}$ of Cu^{2+} species from the coordinated Cu center in Por-COF-Cu, and no the Cu^+ and Cu^0 state were observed in XPS (Fig. S7).

In order to verify the formation of covalent bonds between NH_2-MWCNT and Por-COF, two model compounds were prepared by solvothermal reaction and mechanical grinding of Por-CHO and NH_2-MWCNT, named as Por-CHO-MWCNT-Reaction and Por-CHO-MWCNT-Grinding, respectively. The FT-IR results show a new peak at 1655 cm^{-1} from stretching vibration peak of C=N appeared for Por-CHO-MWCNT-Reaction and Por-CHO-MWCNT-Grinding in comparison with NH_2-MWCNT (Fig. S8). Compared to Por-CHO-MWCNT-Grinding, the relative intensity of C=N stretching vibration peak of Por-CHO-MWCNT-Reaction is higher demonstrating that solvothermal reaction is more prone to the formation C=N by Schiff-base reaction of Por-CHO and NH_2-MWCNT. In the XPS spectra, the peak of N 1 s in C=N of Por-CHO-MWCNT-Reactionis is significantly higher than that of Por-CHO-MWCNT-Grinding and NH_2-MWCNT (Fig. S9), indicating the formation of new C=N bonds by the reaction of Por-CHO and NH_2-MWCNT in this reaction condition. The formation of C=N bonds in Por-CHO-MWCNT-Reaction supports the covalent connection of NH_2-MWCNT and Por-COF in MWCNT-Por-COF.

3.2. Morphology and porosity structural characterization

The morphology of MWCNT-Por-COF-M was characterized by scanning electron microscopy (SEM) and transmission electron microscopy (TEM). The NH_2-MWCNT presents typical nanotube morphology with a smooth surface (Fig. 1b). The pure Por-COF shows sheet-like nanocrystals around 30 nm which were seriously aggregated together (Fig. 1c). As presented in Fig. 1d, the nanocrystals of Por-COF were uniformly anchored on the surface of CNT in MWCNT-Por-COF. The results of TEM measurement for MWCNT-Por-COF further confirm Por-COF was grown surround CNT with uniform dispersion by the in-situ reaction (Fig. 1e). Moreover, the porous Por-COF nanosheets were anchored on MWCNT with the edge of (100) plane (Fig. 1e inset). For comparison, we also synthesized non-covalently connected MWCNT@Por-COF with MWCNT (without modified –NH_2 groups) as precursor. The SEM image of MWCNT@Por-COF shows Por-COF and MWCNT mainly exist separately (Fig. S10). These results demonstrate the essential role of modified –NH_2 groups on NH_2-MWCNT for the dispersion of Por-COF on MWCNT and avoiding the aggregation of Por-COF in the resultant composites. After the coordination of metal ions, the morphology of the series of MWCNT-Por-COF-M have no apparent change as confirmed by SEM (Fig. S11). SEM and TEM images of MWCNT-Por-COF-Cu show the same morphology as the above MWCNT-Por-COF-M (Co, Ni, Fe) (Fig. S12). Furthermore, the elemental mapping and energy dispersive spectroscopy (EDS) for MWCNT-Por-COF-Co were detected. The results show that N and Co elements were uniformly distributed on the CNT (Figs. 1f-1i), and the content of Co element was 1.9 wt% in the EDS, which was lower than theoretical value (6.3 wt%) (Fig. S13). The porosity structural of Por-COF and MWCNT-Por-COF-M were investigated by N_2 absorption and desorption curves at 77 K. The results indicate that all the samples exhibit type I absorption isotherms (Fig. S14-S15) and the pore size distributions are concentrated on 15 Å, similar to that reported previously (Fig. S16) [38].

3.3. Electrocatalytic CO_2RR performances in H-type cell

The electrocatalytic CO_2RR performances for MWCNT-Por-COF-M (M: Co, Ni, Fe) were evaluated in gas-tight H-type electrochemical cell (separated by a Nafion@117 proton exchange membrane) with CO_2-saturated 0.5 M $KHCO_3$ as electrolyte. Before measurements, MWCNT-Por-COF-M were immersed in 0.5 M $KHCO_3$ aqueous solution for 50 h, the identical PXRD patterns before and after immersed demonstrate their structural stability at this condition (Fig. S17). The results of Faradic efficiency for MWCNT-Por-COF-Co support that the different content of NH_2-MWCNT as precursor is the optimism ratio for the electrocatalytic activity of the resultant composites (Fig. S18). For different MWCNT-Por-COF-M, Linear sweep voltammetry (LSV) curves show that MWCNT-Por-COF-Co possesses the smallest onset potential and large current density in CO_2-saturated $KHCO_3$ than that of MWCNT-Por-COF-Ni and MWCNT-Por-COF-Fe (Fig. 2a), demonstrating its much higher CO_2RR activity. In addition, compared to the condition of Ar-saturated $KHCO_3$ solution, the MWCNT-Por-COF-Co shows a much higher current density and smaller onset potential in CO_2-saturated $KHCO_3$ solution (Fig. S19), indicating higher CO_2RR reaction activity than HER [50,51]. To evaluate the selectivity of MWCNT-Por-COF-M for CO_2RR, the reduction products were analyzed by gas chromatography (GC) and Ion chromatography. The results show that CO is the primary reduction product accompanied by a small amount of H_2 from reduced water and there is no detected liquid product by Ion chromatography (Fig. S20-S21). Subsequently, the corresponding Faradic efficiency of CO and H_2 are calculated at − 0.5 to − 1.0 V to further evaluate the electrocatalytic CO_2RR selectivity of the MWCNT-Por-COF-M. As shown in Fig. 2b and S22, the MWCNT-Por-COF-Co showed the best electrocatalytic activity for CO_2-to-CO conversion with the highest CO Faradaic efficiency (FE_{CO}) of 99.3% at − 0.6 V, which was obviously higher than that of MWCNT-Por-COF-Fe (42.1%), MWCNT-Por-COF-Ni (56.4%) and individual Por-COF-Co (1.6%) at the same potential. Furthermore, the MWCNT-Por-COF-Co also maintains excellent FE_{CO} (> 90%) at − 0.6 to − 0.9 V, which outperforms many reported COF-based materials (Table S1) [36–38,40,52–54]. Moreover, the energy efficiency (EE) of MWCNT-Por-COF-Co was calculated to evaluate the energy conversion efficiency in CO_2RR process. The result shows MWCNT-Por-COF-Co displays the largest EE of 87.62% at − 0.6 V attributed to lower overpotential in the CO_2RR process (Fig. S23).

To confirm the contribution of covalent connection between MWCNT and Por-COF to the improved electrocatalytic activity of MWCNT-Por-COF-Co, the electrocatalytic CO_2RR activities of MWCNT@Por-COF-Co without covalent bonds connection and physical mixing sample of NH_2-MWCNT and Por-COF-Co were determined (Fig. S24-S25). The results show covalently connected MWCNT-Por-COF-Co exhibits apparently higher FE_{CO} (99.3%) for CO_2-to-CO conversion than that of non-covalently connected MWCNT@Por-COF-Co (76.8%) and NH_2-MWCNT/Por-COF-Co (46.3%). Thus, the excellent electrocatalytic CO_2RR activity of MWCNT-Por-COF-Co should be attributed to the contribution of covalent connection between CNT and Por-COF which not only ensure the uniform distribution of Por-COF on CNT, but also enables the fluent transfer of electrons from CNT to metal active sites along covalently connected porphyrin planes. The partial current density of CO was carried out to deeply understand the efficiency of MWCNT-Por-COF-M for electrocatalytic CO_2RR. As shown in Fig. 2c, the MWCNT-Por-COF-Co displays a current density of − 18.77 mA cm^{-2} at − 1.0 V, which is much higher than that of MWCNT-Por-COF-Ni (−1.95 mA cm^{-2}), MWCNT-Por-COF-Fe (−5.77 mA cm^{-2}) and individual Por-COF-Co (0.05 mA cm^{-2}). In addition, the turnover frequency (TOF) of MWCNT-Por-COF-Co was calculated to be 70.6 s^{-1} at − 1.0 V, which is also superior to MWCNT-Por-COF-Ni, MWCNT-Por-COF-Fe and individual Por-COF-Co (Fig. 2d). Besides, the ^{13}C-issotopic tracer experiment was carried out to reveal the carbon source of CO under the same reaction conditions. The products were analyzed by gas chromatography-mass spectrometry (GC-MS). The
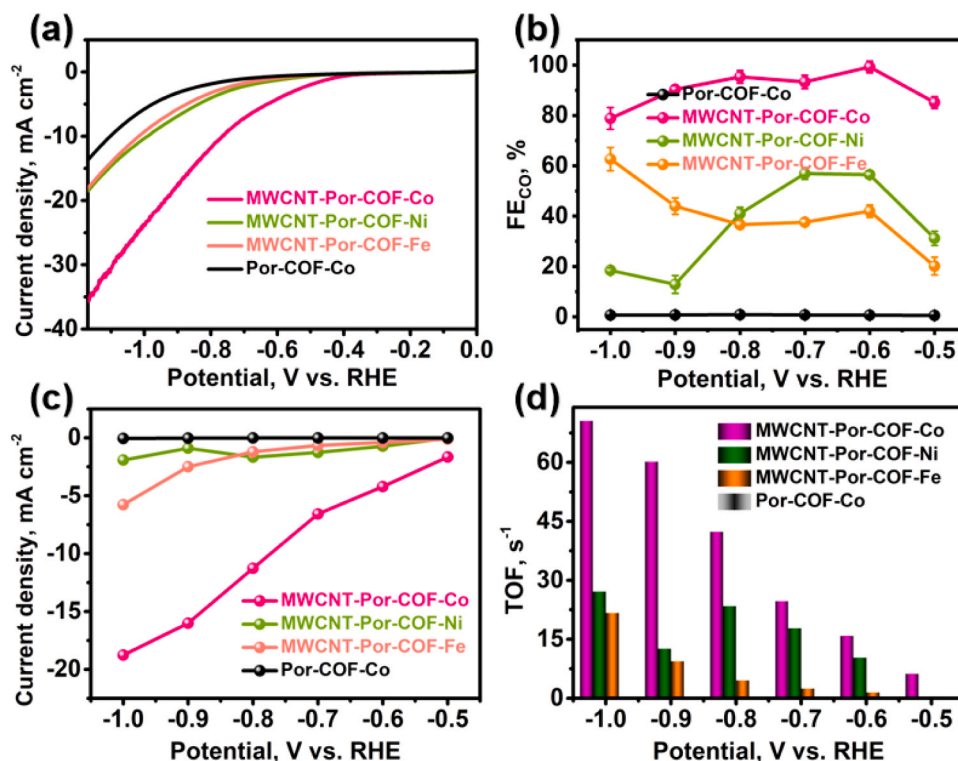
Fig. 2. (a) LSV curves, (b) The FE of CO calculated potential ranges from -0.5 to -1.0 V, (c) The partial current density of CO, and (d) TOFs at different potentials for Por-COF and MWCNT-Por-COF-M (M: Co, Ni, Fe).

result shows the peak at $m/z = 29$ is distributed to ^{13}CO, revealed that the carbon source of CO come from CO_2 molecules in the electrocatalytic process (Fig. 3a).

To elucidate the reaction kinetics activity of MWCNT-Por-COF-M for electrochemical CO_2RR, Tafel slopes were calculated. As presented in Fig. 3b, the Tafel slope of MWCNT-Por-COF-Co is calculated to be 319 mV dec^{-1}, which is much smaller than that of MWCNT-Por-COF-Ni (468 mV dec^{-1}) and MWCNT-Por-COF-Fe (541 mV dec^{-1}). The result indicates the favorable kinetics of MWCNT-Por-COF-Co for the CO_2-to-CO conversion attributed to more efficient charge transfer during CO_2RR process. Moreover, electrochemical double-layer capacitance (C_{dl}) was calculated by measuring cyclic voltammetry (CV) curves in the non-faradaic region with different scan rates (10–100 mV s^{-1}) to evaluate the electrochemical active surface area (ECSA) (Fig. S26-S28). As presented in Fig. 3c, MWCNT-Por-COF-Co exhibits the largest C_{dl} of 21.8 mF cm^{-2} than MWCNT-Por-COF-Ni (15.7 mF cm^{-2}) and MWCNT-Por-COF-Fe (17.6 mF cm^{-2}), indicating that MWCNT-Por-COF-Co has a larger electrochemical area, which might provide more efficient active sites for electrocatalytic CO_2RR. Furthermore, covalently connected MWCNT-Por-COF-Co exhibits the larger C_{dl} than MWCNT@Por-COF-Co (14.8 mF cm^{-2}) without covalent bonds connection (Fig. S29-S30), indicating more metal centers of MWCNT-Por-COF-Co can be excited in during electrocatalytic CO_2RR process.

In order to better understand the CO_2RR kinetics, electrochemical impedance spectroscopy (EIS) measurements were tested. As shown in Fig. 3d, MWCNT-Por-COF-Co displays much smaller charge transfer resistance (10.1 Ω) compared to MWCNT-Por-COF-Ni (208.5 Ω) and MWCNT-Por-COF-Fe (71.9 Ω). This demonstrates a faster charge transfer kinetics exist in the MWCNT-Por-COF-Co, which is favorable for the electrocatalytic CO_2RR performance. Furthermore, CO_2 adsorption isotherms of MWCNT-Por-COF-M were measured (Fig. S31). The results show that the adsorption capacity of MWCNT-Por-COF-Co (8.86 cm^3 g^{-1}) is higher than that of MWCNT-Por-COF-Ni (7.37 cm^3 g^{-1}) and MWCNT-Por-COF-Fe (4.61 cm^3 g^{-1}) (298 K), demonstrating that different metal centers show different CO_2 adsorption capacity, in

accordance with above experiment results. The long-term CO_2RR stability of the MWCNT-Por-COF-Co was examined using current-time (*i-t*) method at -0.7 V in 0.5 M KHCO$_3$. As shown in Fig. 3e, small current density fluctuations and FE$_{CO}$ is detected up to 50 h (CO is analyzed by GC). Moreover, the corresponding FE$_{CO}$ can be maintained at values of ~90%, which indicates that MWCNT-Por-COF-Co possesses prominent stability during the CO_2RR process.

3.4. Electrocatalytic CO_2RR performances in flow cell

To further demonstrate the effect of different metal centers on CO_2 reduction products, The MWCNT-Por-COF-Cu was determined for CO_2RR activity. The electrocatalytic CO_2RR performances for MWCNT-Por-COF-Cu were firstly evaluated in CO_2-saturated 0.5 M KHCO$_3$ aqueous solution through H-type electrochemical cell, and the results show only hydrogen is produced and nothing else was detected. However, when changed to three-compartment flow cell with MWCNT-Por-COF-Cu modified carbon paper electrode as the working electrode and 1.0 M KOH as electrolyte, CH$_4$, C$_2$H$_4$ and CO products were detected in reaction system at a wide potential from -0.7 V to -1.2 V vs. RHE. For MWCNT-Por-COF-Cu, CH$_4$ is regarded as the dominant product with the highest FE$_{CH4}$ of 71.2% at -1.0 V, along with 4.1% FE$_{C2H4}$ and 2.1% FE$_{CO}$ (Figs. 4a-4b and S32). In comparison with MWCNT-Por-COF-Cu, Por-COF-Cu merely displayed weak CO_2RR activity with the FE$_{CH4}$ of 40.8% at -1.1 V and 59.0% FE$_{H2}$. Furthermore, the electrocatalytic CO_2 conversion to CH$_4$ activity of MWCNT-Por-COF-Cu is comparable to that some reported Cu-based catalysts (Table S2) [55–60]. The long-time durability tests of MWCNT-Por-COF-Cu was assessed at -1.0 V in 1.0 M KOH (Fig. S33), the corresponding FE$_{CH4}$ can be retained at values ~70% in 1 h test, which proved the stability of MWCNT-Por-COF-Cu during the CO_2RR process. Besides, to verify the carbon source of CO_2RR products, the isotopic experiment was performed by using $^{13}CO_2$ as carbon source and the products were analyzed by gas chromatography and mass spectra. A peak at $m/z = 17$ from $^{13}CH_4$ (Fig. S34) could be observed in MS spectrum, indicating the carbon sources of CH$_4$
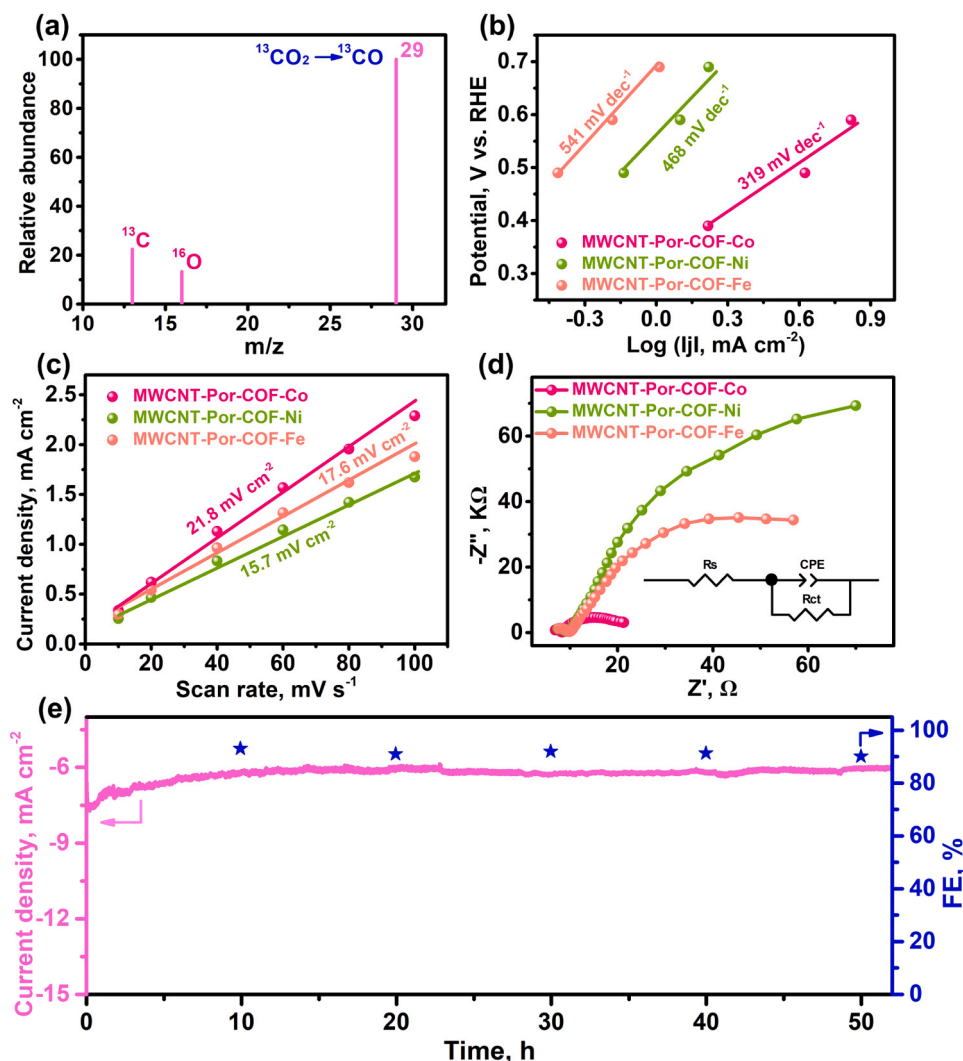
Fig. 3. (a) The GC-MS test of MWCNT-Por-COF-Co of ^{13}CO recorded under $^{13}CO_2$ atmosphere. (b) Tafel slopes, (c) Cdl, and (d) EIS curves for MWCNT-Por-COF-M (M: Co, Ni, Fe). (e) Long-term stability test of MWCNT-Por-COF-Co at -0.7 V.
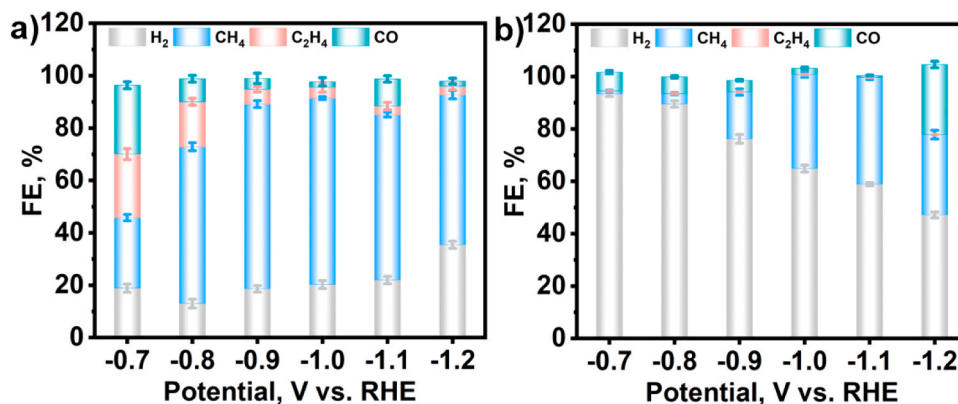
Fig. 4. Electrocatalytic performance of MWCNT-Por-COF-Cu (a) and Por-COF-Cu (b) at different applied potentials (-0.7 to -1.2 V).

indeed derive from the CO_2.

3.5. Mechanism analysis

Based on the above analysis and previously reported works [36,39], a feasible mechanism was proposed for MWCNT-Por-COF-M (Co, Ni, Fe)

(Fig. S35). In the electrocatalytic CO_2-to-CO process, CNT acts as conductive platform improving the electron transfer in the material. Thanks to the covalent connection between CNT and Pro-COF-M (Co, Ni, Fe) as well as the vertical integration mode of them, electrons in CNT could continuously transfer to porphyrin plane of Pro-COF-M (Co, Ni, Fe) via connected covalent bonds. For the electronic character of

porphyrin and conjugated structure in Pro-COF-M (Co, Ni, Fe) layer, the electrons could be fluently transmitted to metal active sites for CO_2 reduction. This combination mode is superior to that without covalent for the dispersion of Pro-COF-M (Co, Ni, Fe) and electrons transfer between interfaces and within Pro-COF-M (Co, Ni, Fe) component, thus leading to largely enhanced electrocatalytic CO_2RR performance.

As for the MWCNT-Por-COF-Cu, in order to further clarify the mechanism of MWCNT-Por-COF-Cu in electrocatalytic CO_2-to-CH_4, the XRD, XPS, Auger spectrum, SEM, TEM and HR-TEM of MWCNT-Por-COF-Cu after electrocatalytic CO_2RR were tested. The PXRD patterns, SEM morphology and XPS spectra of MWCNT-Por-COF-Cu are no obvious change before and after electrocatalytic CO_2RR (Fig. S36-S37, S38a-b). However, ultra-small particles (ca. 2 nm) with the lattice fringe of 0.21 nm could be observed in the high-resolution TEM image (Fig. S38c-d) [61], corresponding to the (111) plane of Cu^0. The Cu LMM Auger spectra (Fig. S39) after CO_2RR shows a peak centered at 567.8 eV corresponding to the Cu^0, while the Cu^+ peak was not obvious. The results of HRTEM and Auger spectrum indicate that Cu^0 species (metallic Cu nanoclusters) may be generated during electrocatalytic CO_2RR test. The Cu ions in MWCNT-Por-COF-Cu were converted in-situ into Copper-based nanoclusters, which act as real active sites for electrocatalytic CO_2-to-CH_4 process, and this mechanism is similar to the reported literatures [58,62]. This restructuring behavior of MWCNT-Por-COF-Cu leads to different catalytic products.

4. Conclusions

In summary, we have explored a new model of covalent connection MWCNT-Por-COF-M for efficient electrocatalytic CO_2-to-CO conversion. This integration could tightly combine Por-COF and CNT together with uniform distribution and controlled electronic transfer pathway in electrocatalytic process. The experiments results showed that MWCNT-Por-COF-M (M: Co, Ni, Fe) composites show higher electrocatalytic activity and Faraday efficiency compared to the pure Por-COF-M. In particular, the MWCNT-Por-COF-Co shows the highest FE_{CO} up to 99.3% at -0.6 V, along with a current density of 18.77 mA cm^{-2} and TOF of 70.6 s^{-1} at -1.0 V. It is clarified that the superior electrocatalytic activity of MWCNT-Por-COF-Co is mainly attributed to more efficient electron transfer for the effective integration mode of components. Besides, we also discussed the electrocatalytic CO_2 reduction activity of MWCNT-Por-COF-Cu in 1.0 M KOH by flow cell. The results show that MWCNT-Por-COF-Cu exhibits the highest CH_4 faradaic efficiency of 71.2% compared to the MWCNT-Por-COF. The results of HRTEM and Auger spectrum revealed that the high performance of MWCNT-Por-COF-Cu could be attributed to the generated Copper-based nanoclusters during the electrocatalytic CO_2RR process. This work provides a new strategy for further wise constructing COF-based composites for efficient electrocatalytic CO_2RR.

CRediT authorship contribution statement

Hong Dong: Conceptualization, Investigation, Writing – review & editing. **Meng Lu:** Writing – review & editing. **Ya Wang:** Formal analysis. **Hong-Liang Tang:** Data curation. **Di Wu:** Data curation. **Xiaojun Sun:** Project administration. **Feng-Ming Zhang:** Supervision, Project administration.

Declaration of Competing Interest

The authors declare that they have no known competing financial interests or personal relationships that could have appeared to influence the work reported in this paper.

Acknowledgments

Appendix A. Supporting information

Supplementary data associated with this article can be found in the online version at doi:10.1016/j.apcatb.2021.120897.

References

[1] J.D. Shakun, P.U. Clark, F. He, S.A. Marcott, A.C. Mix, Z. Liu, B. Otto-Bliesner, A. Schmittner, E. Bard, Global warming preceded by increasing carbon dioxide concentrations during the last deglaciation, Nature 484 (2012) 49–54.

[2] T.A. Jacobson, J.S. Kler, M.T. Hernke, R.K. Braun, K.C. Meyer, W.E. Funk, Direct human health risks of increased atmospheric carbon dioxide, Nat. Sustain. 2 (2019) 691–701.

[3] S.J. Davis, K. Caldeira, H.D. Matthews, Future CO_2 emissions and climate change from existing energy infrastructure, Science 329 (2010) 1330–1333.

[4] Y. Hou, Y.L. Liang, P.C. Shi, Y.B. Huang, R. Cao, Atomically dispersed Ni species on N-doped carbon nanotubes for electroreduction of CO_2 with nearly 100% CO selectivity, Appl. Catal., B 271 (2020), 118929.

[5] J.D. Yi, D.H. Si, R.K. Xie, Q. Yin, M.D. Zhang, Q. Wu, G.L. Chai, Y.B.A. Huang, R. Cao, Conductive two-dimensional phthalocyanine-based metal-organic framework nanosheets for efficient electroreduction of CO_2, Angew. Chem., Int. Ed. 60 (2021) 17108–17114.

[6] Y.H. Zou, Y.B. Huang, D.H. Si, Q. Yin, Q.J. Wu, Z.X. Weng, R. Cao, Porous metal–organic framework liquids for enhanced CO2adsorption and catalytic conversion, Angew. Chem., Int. Ed. 60 (2021) 20915–20920.

[7] J. Qiao, Y. Liu, F. Hong, J. Zhang, A review of catalysts for the electroreduction of carbon dioxide to produce low-carbon fuels, Chem. Soc. Rev. 43 (2014) 631–675.

[8] T. Burdyny, W.A. Smith, CO2reduction on gas-diffusion electrodes and why catalytic performance must be assessed at commercially-relevant conditions, Energy Environ. Sci. 12 (2019) 1442–1453.

[9] D.-H. Nam, P. De Luna, A. Rosas-Hernández, A. Thevenon, F. Li, T. Agapie, J. C. Peters, O. Shekhah, M. Eddaoudi, E.H. Sargent, Molecular enhancement of heterogeneous CO_2 reduction, Nat. Mater. 19 (2020) 266–276.

[10] P. De Luna, C. Hahn, D. Higgins, S.A. Jaffer, T.F. Jaramillo, E.H. Sargent, What would it take for renewably powered electrosynthesis to displace petrochemical processes? Science 364 (2019) eaav3506.

[11] C.-T. Dinh, T. Burdyny, M.G. Kibria, A. Seifitokaldani, C.M. Gabardo, F.P.G. De Arquer, A. Kiani, J.P. Edwards, P. De Luna, O.S. Bushuyev, CO_2 electroreduction to ethylene via hydroxide-mediated copper catalysis at an abrupt interface, Science 360 (2018) 783–787.

[12] Q. Wu, M.J. Mao, Q.J. Wu, J. Liang, Y.B. Huang, R. Cao, Construction of donor–acceptor heterojunctions in covalent organic framework for enhanced CO2 electroreduction, Small 17 (2021), 2004933.

[13] Q. Wu, J. Liang, Z.-L. Xie, Y.-B. Huang, R. Cao, Spatial sites separation strategy to fabricate atomically isolated nickel catalysts for efficient CO2 electroreduction, ACS Mater. Lett. 3 (2021) 454–461.

[14] M.D. Zhang, D.H. Si, J.D. Yi, Q. Yin, Y.B. Huang, R. Cao, Conductive phthalocyanine-based metal-organic framework as a highly efficient electrocatalyst for carbon dioxide reduction reaction, Sci. China-Chem. 64 (2021) 1332–1339.

[15] Y. Hou, Y.-B. Huang, Y.-L. Liang, G.-L. Chai, J.-D. Yi, T. Zhang, K.-T. Zang, J. Luo, R. Xu, H. Lin, S.-Y. Zhang, H.-M. Wang, R. Cao, Unraveling the reactivity and selectivity of atomically isolated metal–nitrogen sites anchored on porphyrinic triazine frameworks for electroreduction of CO_2, CCS Chem. 1 (2019) 384–395.

[16] W.F. Xiong, H.F. Li, H.H. You, M.N. Cao, R. Cao, Encapsulating metal organic framework into hollow mesoporous carbon sphere as efficient oxygen bifunctional electrocatalyst, Natl. Sci. Rev. 7 (2020) 609–619.

[17] J.H. Wu, Y. Huang, W. Ye, Y.G. Li, CO_2 reduction: from the electrochemical to photochemical approach, Adv. Sci. 4 (2017), 1700194.

[18] Y.-J. Qiao, V. Sethuraman, R. Michalsky, A.A. Peterson, TiO2-assisted photoisomerization of azo dyes using self-assembled monolayers: case study on para-methyl red towards solar-cell applications, ACS Catal. 4 (2014) 3742–3748.

[19] D.D. Zhu, J.L. Liu, S.Z. Qiao, Recent advances in inorganic heterogeneous electrocatalysts for reduction of carbon dioxide, Adv. Mater. 28 (2016) 3423–3452.

[20] Q. Li, J. Fu, W. Zhu, Z. Chen, B. Shen, L. Wu, Z. Xi, T. Wang, G. Lu, J.-j. Zhu, Tuning Sn-catalysis for electrochemical reduction of CO_2 to CO via the core/shell Cu/SnO2 structure, J. Am. Chem. Soc. 139 (2017) 4290–4293.

[21] W. Luc, X. Fu, J. Shi, J.-J. Lv, M. Jouny, B.H. Ko, Y. Xu, Q. Tu, X. Hu, J. Wu, Two-dimensional copper nanosheets for electrochemical reduction of carbon monoxide to acetate, Nat. Catal. 2 (2019) 423–430.

[22] M. Asadi, K. Kim, C. Liu, A.V. Addepalli, P. Abbasi, P. Yasaei, P. Phillips, A. Behranginia, J.M. Cerrato, R. Haasch, Nanostructured transition metal dichalcogenide electrocatalysts for CO_2 reduction in ionic liquid, Science 353 (2016) 467–470.

[23] H. Jung, S.Y. Lee, C.W. Lee, M.K. Cho, D.H. Won, C. Kim, H.-S. Oh, B.K. Min, Y. J. Hwang, Electrochemical fragmentation of Cu2O nanoparticles enhancing

selective C-C coupling from CO_2 reduction reaction, J. Am. Chem. Soc. 141 (2019) 4624–4633.

[24] S. Guo, S. Zhao, X. Wu, H. Li, Y. Zhou, C. Zhu, N. Yang, X. Jiang, J. Gao, L. Bai, A Co3O4-CDots-C3N4 three component electrocatalyst design concept for efficient and tunable CO_2 reduction to syngas, Nat. Commun. 8 (2017) 1828.

[25] C. Ding, C. Feng, Y. Mei, F. Liu, H. Wang, M. Dupuis, C. Li, Appl. Catal., B ((2019), 118391.

[26] Q. Wang, J. Wang, J.C. Wang, X. Hu, Y. Bai, X.H. Zhong, Z.Q. Li, Coupling CsPbBr3 quantum dots with covalent triazine frameworks for visible-light-driven CO_2 reduction, ChemSusChem 14 (2021) 1131–1139.

[27] J.W. Fu, K.X. Jiang, X.Q. Qiu, J.G. Yu, M. Liu, Product selectivity of photocatalytic CO_2 reduction reactions, Mater. Today 32 (2020) 222–243.

[28] N. Huang, X. Chen, R. Krishna, D. Jiang, Two-dimensional covalent organic frameworks for carbon dioxide capture through channel-wall functionalization, Angew. Chem., Int. Ed. 54 (2015) 2986–2990.

[29] H. Furukawa, O.M. Yaghi, Storage of hydrogen, methane, and carbon dioxide in highly porous covalent organic frameworks for clean energy applications, J. Am. Chem. Soc. 131 (2009) 8875–8883.

[30] S.-Y. Ding, M. Dong, Y.-W. Wang, Y.-T. Chen, H.-Z. Wang, C.-Y. Su, W. Wang, Thioether-based fluorescent covalent organic framework for selective detection and facile removal of mercury(II), J. Am. Chem. Soc. 138 (2016) 3031–3037.

[31] Q. Fang, J. Wang, S. Gu, R.B. Kaspar, Z. Zhuang, J. Zheng, H. Guo, S. Qiu, Y. Yan, 3D porous crystalline polyimide covalent organic frameworks for drug delivery, J. Am. Chem. Soc. 137 (2015) 8352–8355.

[32] G. Zhang, X. Li, Q. Liao, Y. Liu, K. Xi, W. Huang, X. Jia, Water-dispersible PEG-curcumin/amine-functionalized covalent organic framework nanocomposites as smart carriers for in vivo drug delivery, Nat. Commun. 9 (2018) 2785.

[33] H. Wang, H. Wang, Z. Wang, L. Tang, G. Zeng, P. Xu, M. Chen, T. Xiong, C. Zhou, X. Li, Covalent organic framework photocatalysts: structures and applications, Chem. Soc. Rev. 49 (2020) 4135–4165.

[34] K. Geng, T. He, R. Liu, K.T. Tan, Z. Li, S. Tao, Y. Gong, Q. Jiang, D. Jiang, Covalent organic frameworks: design, synthesis, and functions, Chem. Rev. 120 (2020) 8814–8933.

[35] S. Kandambeth, K. Dey, R. Banerjee, Covalent organic frameworks: chemistry beyond the structure, J. Am. Chem. Soc. 141 (2018) 1807–1822.

[36] Q. Wu, R.-K. Xie, M.-J. Mao, G.-L. Chai, J.-D. Yi, S.-S. Zhao, Y.-B. Huang, R. Cao, The COPD-readmission (CORE) score: a novel prediction model for one-year chronic obstructive pulmonary disease readmissions, ACS Energy Lett. 5 (2020) 1005–1012.

[37] H. Liu, J. Chu, Z. Yin, X. Cai, L. Zhuang, H. Deng, Covalent organic frameworks linked by amine bonding for concerted electrochemical reduction of CO_2, Chem 4 (2018) 1696–1709.

[38] C.S. Diercks, S. Lin, N. Kornienko, E.A. Kapustin, E.M. Nichols, C. Zhu, Y. Zhao, C. J. Chang, O.M. Yaghi, Reticular electronic tuning of porphyrin active sites in covalent organic frameworks for electrocatalytic carbon dioxide reduction, J. Am. Chem. Soc. 140 (2018) 1116–1122.

[39] H.-J. Zhu, M. Lu, Y.-R. Wang, S.-J. Yao, M. Zhang, Y.-H. Kan, J. Liu, Y. Chen, S.-L. Li, Y.-Q. Lan, Efficient electron transmission in covalent organic framework nanosheets for highly active electrocatalytic carbon dioxide reduction, Nat. Commun. 11 (2020) 497.

[40] S. Lin, C.S. Diercks, Y.-B. Zhang, N. Kornienko, E.M. Nichols, Y. Zhao, A.R. Paris, D. Kim, P. Yang, O.M. Yaghi, Covalent organic frameworks comprising cobalt porphyrins for catalytic CO_2 reduction in water, Science 349 (2015) 1208–1213.

[41] N. Huang, K.H. Lee, Y. Yue, X.Y. Xu, S. Irle, Q.H. Jiang, D.L. Jiang, A stable and conductive metallophthalocyanine framework for electrocatalytic carbon dioxide reduction in water, Angew. Chem., Int. Ed. 59 (2020) 16587–16593.

[42] Y. Lu, J. Zhang, W. Wei, D.-D. Ma, X.-T. Wu, Q.-L. Zhu, Efficient carbon dioxide electroreduction over ultrathin covalent organic framework nanolayers with isolated cobalt porphyrin units, ACS Appl. Mater. Interfaces 12 (2020) 37986–37992.

[43] A. Moya, M. Hernando-Pérez, M. Pérez-Illana, C. San Martín, J. Gómez-Herrero, J. Alemán, R. Mas-Ballesté, P.J. de Pablo, Multifunctional carbon nanotubes covalently coated with imine-based covalent organic frameworks: exploring structure-property relationships through nanomechanics, Nanoscale 12 (2020) 1128–1137.

[44] A.A. Balandin, Thermal properties of graphene and nanostructured carbon materials, Nat. Mater. 10 (2011) 569–581.

[45] B. Sun, J. Liu, A. Cao, W. Song, D. Wang, Interfacial synthesis of ordered and stable covalent organic frameworks on amino-functionalized carbon nanotubes with enhanced electrochemical performance, Chem. Commun. 53 (2017) 6303–6306.

[46] X.M. Hu, M.H. Rønne, S.U. Pedersen, T. Skrydstrup, K. Daasbjerg, Enhanced catalytic activity of cobalt porphyrin in CO_2 electroreduction upon immobilization on carbon materials, Angew. Chem., Int. Ed. 56 (2017) 6468–6472.

[47] Y. Wu, Z. Jiang, X. Lu, Y. Liang, H. Wang, Domino electroreduction of CO_2 to methanol on a molecular catalyst, Nature 575 (2019) 639–642.

[48] X. Zhang, Z. Wu, X. Zhang, L. Li, Y. Li, H. Xu, X. Li, X. Yu, Z. Zhang, Y. Liang, Highly selective and active CO_2 reduction electrocatalysts based on cobalt phthalocyanine/carbon nanotube hybrid structures, Nat. Commun. 8 (2017) 14675.

[49] H. Liao, H. Wang, H. Ding, X. Meng, H. Xu, B. Wang, X. Ai, C. Wang, A 2D porous porphyrin-based covalent organic framework for sulfur storage in lithium–sulfur batteries, J. Mater. Chem. A 4 (2016) 7416–7421.

[50] C. Cao, D.-D. Ma, J.-F. Gu, X. Xie, G. Zeng, X. Li, S.-G. Han, Q.-L. Zhu, X.-T. Wu, Q. Xu, Metal–organic layers leading to atomically thin bismuthene for efficient carbon dioxide electroreduction to liquid fuel, Angew. Chem., Int. Ed. 59 (2020) 15014–15020.

[51] Y.R. Wang, R.X. Yang, Y.F. Chen, G.K. Gao, Y.J. Wang, S.L. Li, Y.Q. Lan, Chloroplast-like porous bismuth-based core–shell structure for high energy efficiency CO_2 electroreduction, Sci. Bull. 65 (2020) 1635–1642.

[52] E.M. Johnson, R. Haiges, S.C. Marinescu, Covalent-organic frameworks composed of rhenium bipyridine and metal porphyrins: designing heterobimetallic frameworks with two distinct metal sites, ACS Appl. Mater. Interfaces 10 (2018) 37919–37927.

[53] D.A. Popov, J.M. Luna, N.M. Orchanian, R. Haiges, C.A. Downes, S.C. Marinescu, A 2,2′-bipyridine-containing covalent organic framework bearing rhenium(i) tricarbonyl moieties for CO_2 reduction, Dalton Trans. 47 (2018) 17450–17460.

[54] X.M. Hu, M.H. Rønne, S.U. Pedersen, T. Skrydstrup, K. Daasbjerg, Enhanced catalytic activity of cobalt porphyrin in CO_2 electroreduction upon immobilization on carbon materials, Angew. Chem. Int. Ed. 56 (2017) 6468–6472.

[55] L. Zhang, X.X. Li, Z.L. Lang, Y. Liu, J. Liu, L. Yuan, W.Y. Lu, Y.S. Xia, L.Z. Dong, D. Q. Yuan, Y.Q. Lan, Enhanced cuprophilic interactions in crystalline catalysts facilitate the highly selective electroreduction of CO2to CH4, J. Am. Chem. Soc. 143 (2021) 3808–3816.

[56] Y.-R. Wang, M. Liu, G.-K. Gao, Y.-L. Yang, R.-X. Yang, H.-M. Ding, Y. Chen, S.-L. Li, Y.-Q. Lan, Implanting numerous hydrogen-bonding networks in a Cu-porphyrin-based nanosheet to boost CH4 selectivity in neutral-media CO2 electroreduction, Angew. Chem., Int. Ed. 60 (2021) 21952–21958.

[57] J.D. Yi, R.K. Xie, Z.L. Xie, G.L. Chai, T.F. Liu, R.P. Chen, Y.B. Huang, R. Cao, Highly selective CO_2 electroreduction to CH4 by insitu generated Cu2 O single-type sites on a conductive MOF: stabilizing key intermediates with hydrogen bonding, Angew. Chem., Int. Ed. 59 (2020) 23641–23648.

[58] Z. Weng, Y.S. Wu, M.Y. Wang, J.B. Jiang, K. Yang, S.J. Huo, X.F. Wang, Q. Ma, G. W. Brudvig, V.S. Batista, Y.Y. Liang, Z.X. Feng, H.L. Wang, Active sites of copper-complex catalytic materials for electrochemical carbon dioxide reduction, Nat. Commun. 9 (2018) 415.

[59] M. Liu, Y.-R. Wang, H.-M. Ding, M. Lu, G.-K. Gao, L.-Z. Dong, Q. Li, Y. Chen, S.-L. Li, Y.-Q. Lan, Self-assembly of anthraquinone covalent organic frameworks as 1D superstructures for highly efficient CO_2 electroreduction to CH4, Sci. Bull. 66 (2021) 1659–1668.

[60] A.X. Guan, Z. Chen, Y.L. Quan, C. Peng, Z.Q. Wang, S.K. Sham, C. Yang, Y.L. Ji, L. P. Qian, X. Xu, G.F. Zheng, Boosting CO2 electroreduction to CH4via tuning neighboring single-copper sites, ACS Energy Lett. 5 (2020) 1044–1053.

[61] D.Z. Zhong, Z.J. Zhao, Q. Zhao, D.F. Cheng, B. Liu, G. Zhang, W.Y. Deng, H. Dong, L. Zhang, J.K. Li, J.P. Li, J.L. Gong, Coupling of Cu(100) and (110) facets promotes carbon dioxide conversion to hydrocarbons and alcohols, Angew. Chem., Int. Ed. 60 (2021) 4879–4885.

[62] B. Mei, C. Liu, J. Li, S. Gu, X. Du, S. Lu, F. Song, W. Xu, Z. Jiang, Operando HERFD-XANES and surface sensitive Δμ analyses identify the structural evolution of copper (II) phthalocyanine for electroreduction of CO_2, J. Energy Chem. 64 (2022) 1–7.